Fermi Non-detections of Four X-Ray Jet Sources and Implications for the IC/CMB Mechanism

Peter Breiding[1], Eileen T. Meyer[1] , Markos Georganopoulos[1,2] , M. E. Keenan[1], N. S. DeNigris[1], and Jennifer Hewitt[1]
[1] Department of Physics, University of Maryland Baltimore County, Baltimore, MD 21250, USA; meyer@umbc.edu
[2] NASA Goddard Space Flight Center, Code 663, Greenbelt, MD 20771, USA
Received 2017 August 1; revised 2017 September 28; accepted 2017 September 28; published 2017 November 6

Abstract

Since its launch in 1999, the *Chandra* X-ray observatory has discovered several dozen X-ray jets associated with powerful quasars. In many cases, the X-ray spectrum is hard and appears to come from a second spectral component. The most popular explanation for the kpc-scale X-ray emission in these cases has been inverse-Compton (IC) scattering of Cosmic Microwave Background (CMB) photons by relativistic electrons in the jet (the IC/CMB model). Requiring the IC/CMB emission to reproduce the observed X-ray flux density inevitably predicts a high level of gamma-ray emission, which should be detectable with the *Fermi* Large Area Telescope (LAT). In previous work, we found that gamma-ray upper limits from the large-scale jets of 3C 273 and PKS 0637−752 violate the predictions of the IC/CMB model. Here, we present *Fermi*/LAT flux density upper limits for the X-ray jets of four additional sources: PKS 1136–135, PKS 1229–021, PKS 1354+195, and PKS 2209+080. We show that these limits violate the IC/CMB predictions at a very high significance level. We also present new *Hubble Space Telescope* observations of the quasar PKS 2209+080 showing a newly detected optical jet, and Atacama Large Millimeter/submillimeter Array band 3 and 6 observations of all four sources, which provide key constraints on the spectral shape that enable us to rule out the IC/CMB model.

Key words: galaxies: active – galaxies: jets

1. Introduction

The first astrophysical target observed by the *Chandra* X-ray Observatory was PKS 0637–752, a relatively distant ($z = 0.651$) radio-loud active galactic nucleus (AGN). Unexpectedly, *Chandra* discovered high levels of X-ray emission associated with the previously known kpc-scale radio jet (Chartas et al. 2000; Schwartz et al. 2000). The *Chandra* observations revealed bright X-ray knots roughly co-spatial with the radio knots, but with an X-ray flux density far too high and an X-ray spectrum far too hard to be consistent with a single radio-optical-X-ray synchrotron spectrum. In the years that followed, this phenomenon of bright X-ray jets in which the X-ray emission could not be explained by an extrapolation of the radio-optical synchrotron spectrum was found to operate in dozens of other sources, nearly always in more powerful jets with a Fanaroff & Riley (FR) type II morphology (see Harris & Krawczynski 2006, for a review).[3] In this paper, we refer to any jet with evidence of multiple spectra as a Multiple Spectral Component or "MSC" jet. Typically, the observed X-ray emission in less-powerful FR I jets is more consistent with a single radio to X-ray synchrotron spectrum (e.g., Wilson & Yang 2002).

In the original papers announcing the detection of the MSC jet associated with PKS 0637–752 by *Chandra*, Chartas et al. (2000) and Schwartz et al. (2000) ruled out thermal bremsstrahlung, synchrotron self-Compton, and inverse Compton off the Cosmic Microwave Background (IC/CMB) from a mildly relativistic kpc-scale jet as the possible X-ray emission mechanisms. However, proper motion studies of PKS 0637 −752 with Very Long Baseline Interferometry (VLBI) had

shown highly superluminal apparent velocities of $11.4 \pm 0.6c$ on parsec scales, suggesting a highly relativistic flow ($\Gamma > 11.4$) and a jet angle to the line of sight less than $8°9$ (Lovell et al. 2000). Independently, both Tavecchio et al. (2000) and Celotti et al. (2001) suggested that the IC/CMB model could produce the required X-ray flux density in PKS 0637−752 if the jet remained highly relativistic on kpc scales ($\Gamma \sim 10$ rather than $\Gamma \sim 1$–2) and was pointed at a small angle with respect to the line of sight. This model has been widely adopted by the community as the probable X-ray emission mechanism for MSC jets (e.g., Sambruna et al. 2002, 2004; Jorstad & Marscher 2006; Miller et al. 2006; Tavecchio et al. 2007; Marshall et al. 2011; Perlman et al. 2011; Kharb et al. 2012; Stanley et al. 2015). While many AGN jets have been shown to be highly relativistic on the sub-pc scale via proper motion studies with VLBI (e.g., Jorstad et al. 2005; Lister et al. 2009), this is no guarantee that they remain so on the kpc scale, with population-based evidence suggesting they are at most mildly relativistic (Mullin & Hardcastle (2009) found $\Gamma \approx 1.18$–1.49 for FR II sources; also see Arshakian & Longair (2004)).

1.1. Problems with the IC/CMB Model

One problematic aspect of the IC/CMB model is that it is energetically costly, with kinetic jet powers at or sometimes exceeding the Eddington luminosity for these sources (Dermer & Atoyan 2004). This is primarily because it requires extending the electron energy distribution to very low energies to provide electrons of the right energy to produce the observed X-ray emission from upscattered infrared CMB photons. This low-energy extension (i.e., a low γ_{min} value) of the electron energy distribution greatly increases the total energy content of the jet by requiring a much larger total number of electrons. While such an extension is possible, there is no direct evidence

---

[3] Here, we use the term FR to refer to the Fanaroff–Riley classification of radio galaxies, where FR I-type sources are of lower radio luminosity and higher surface brightnesses toward the core than the FR II type sources that typically terminate in bright "hot spots" (Fanaroff & Riley 1974).

for these low-energy electrons because their synchrotron radiation would be at frequencies much less than our GHz-frequency radio observations.

The radiative losses of the electrons responsible for the X-ray emission are very weak in the IC/CMB model, with radiative lifetimes in excess of 10^6 years (Harris & Krawczynski 2006). In the simplest case, we would thus expect continuous X-ray emission along the entire jet length rather than the observed X-ray knots noted by Atoyan & Dermer (2004) and Stawarz et al. (2004). This problem can be avoided if the X-ray emitting plasma is confined to moving blobs rather than a continuous jet flow (Tavecchio et al. 2003). This solution would require these X-ray emitting blobs to be propagating with a high Γ, which may be observable with proper motion studies for nearby sources. However, in the case of 3C 273, Meyer et al. (2016) found that the knots are stationary, with a limit of apparent speed $\beta_{app} < 1c$, corresponding to a limit of $\Gamma < 2.9$, which is incompatible with the IC/CMB interpretation for the X-rays.

A feature of some of these MSC jets is offsets in peak brightness between radio, optical, and X-ray wavelengths when observed with similar angular resolutions (see the case of 3C 111 in Clautice et al. (2016) for a clear example of this). There is no reasonable explanation for these offsets in the IC/CMB model because they are inconsistent with the idea that the X-ray, radio, and optical emission is produced by the same population of relativistic electrons, where we would expect co-spatial emission regions.

In addition to the above difficulties, there have been several observations of MSC jets that directly challenge the IC/CMB model. *Hubble Space Telescope* (*HST*) polarization measurements of the rising UV-component in the jet of PKS 1136–135, clearly part of the second spectral component, show fractional polarization measures in excess of 30% for several knots (Cara et al. 2013). Because IC/CMB emission is expected to have very low polarization (see Uchiyama 2008; McNamara et al. 2009), it is extremely unlikely that the second component is produced by the IC/CMB mechanism in this source. Another recent study by Hardcastle et al. (2016) of the nearby FR II radio galaxy Pictor A shows IC/CMB to be incompatible with the observed jet to counter-jet flux ratio. They found a ratio orders of magnitude less than what would be expected if IC/CMB were the source of the X-rays (in which case, $\Gamma \geqslant 5$ and a jet angle less than a few degrees is required). While the conclusions drawn from these observations of PKS 1136–135, 3C 273, and Pictor A do not necessarily apply to all MSC jets, they already necessitate a second emission mechanism, other than IC/CMB, to explain the X-ray emission in these cases.

There are several alternative models that might explain the MSC jets. In particular, a second population of synchrotron-emitting electrons (Atoyan & Dermer 2004; Harris et al. 2004; Kataoka & Stawarz 2005; Hardcastle 2006; Jester et al. 2006; Uchiyama et al. 2006) and various hadronic emission models (Aharonian 2002; Kusunose & Takahara 2017; Petropoulou et al. 2017). Until recently, it has been difficult to reject the IC/CMB model in favor of any alternative, because in most cases any model can be tuned to reproduce the somewhat sparsely sampled spectral energy distribution (SED). However, the question of which emission process is at work in these X-ray jets is important because these models imply vastly different physical properties.

In the case of the second synchrotron model, it will be important to understand why there are multiple electron energy distributions and how this is connected to the particle acceleration taking place in these jets. An immediate consequence of a higher-energy electron distribution is subsequent TeV gamma-rays produced when these electrons IC scatter the CMB (Georganopoulos et al. 2006; Meyer et al. 2015). These TeV gamma-rays may be detectable for low-redshift sources with the upcoming Cherenkov Telescope Array (CTA). Alternatively, if the source of the X-rays is due to hadronic emission processes, then this has important implications for the particle make-up and energy content of these jets.

1.2. Using the Fermi/Large Area Telescope (LAT) to Test the IC/CMB Model

As noted by Georganopoulos et al. (2006), the IC/CMB model predicts a high level of IC/CMB gamma-ray emission from the jet, which should be detectable with the *Fermi*/LAT. In previous work, we developed a technique to search for the steady gamma-ray IC/CMB emission component at times when the variable core was in a low state, necessary because the resolution of *Fermi* is insufficient to separately resolve the core and jet. This technique was applied in 3C 273 (Meyer & Georganopoulos 2014) and PKS 0637–752 (Meyer et al. 2015, 2017), where in both cases the upper limits to the gamma-ray flux during times when the core was quiescent were well below the required level from IC/CMB. This paper follows these works for four more MSC jets where the X-ray emission has been previously modeled as due to IC/CMB. However, in this paper we have targeted sources which are not detected in the *Fermi*/LAT 3FGL four-year point source catalog, which strongly suggests that the gamma-ray emission expected under the IC/CMB model may be absent, without any complication of gamma-ray emission from the core. Additional MSC jets are currently being analyzed in order to establish which sources may be consistent with the IC/CMB model based on gamma-ray observations, but the presence of newly detected point sources in the region of interest (ROI) makes the analysis more complicated, and we leave the discussion of these sources to a future paper.

In Section 2, we present the new and archival radio and optical data analyzed for our four targets, as well as the method of deriving *Fermi* upper limits. In Section 3, we present the resulting limits, which clearly violate the expectations of the IC/CMB model. In Section 4, we discuss the properties of the small but growing sample of MSC jets in which IC/CMB has been ruled out, including several lines of evidence that suggest they are not extremely well-aligned, as required under the IC/CMB model. Finally, in Section 5 we summarize our findings.

2. Data Analysis

2.1. Sample Properties

In Table 1, we summarize the source properties of the four targets presented in this paper and the two sources in which the IC/CMB model for the X-rays has already been ruled out, PKS 0637–752 and 3C 273. In columns 2–4, we report the source redshift and corresponding angular size scale in kpc per arcsecond, and the black hole mass as M_{BH}, taken from the literature where available (as noted in the table). Using data from NED, we decomposed the radio spectrum of these sources into the extended (isotropic) "lobe" component and beamed
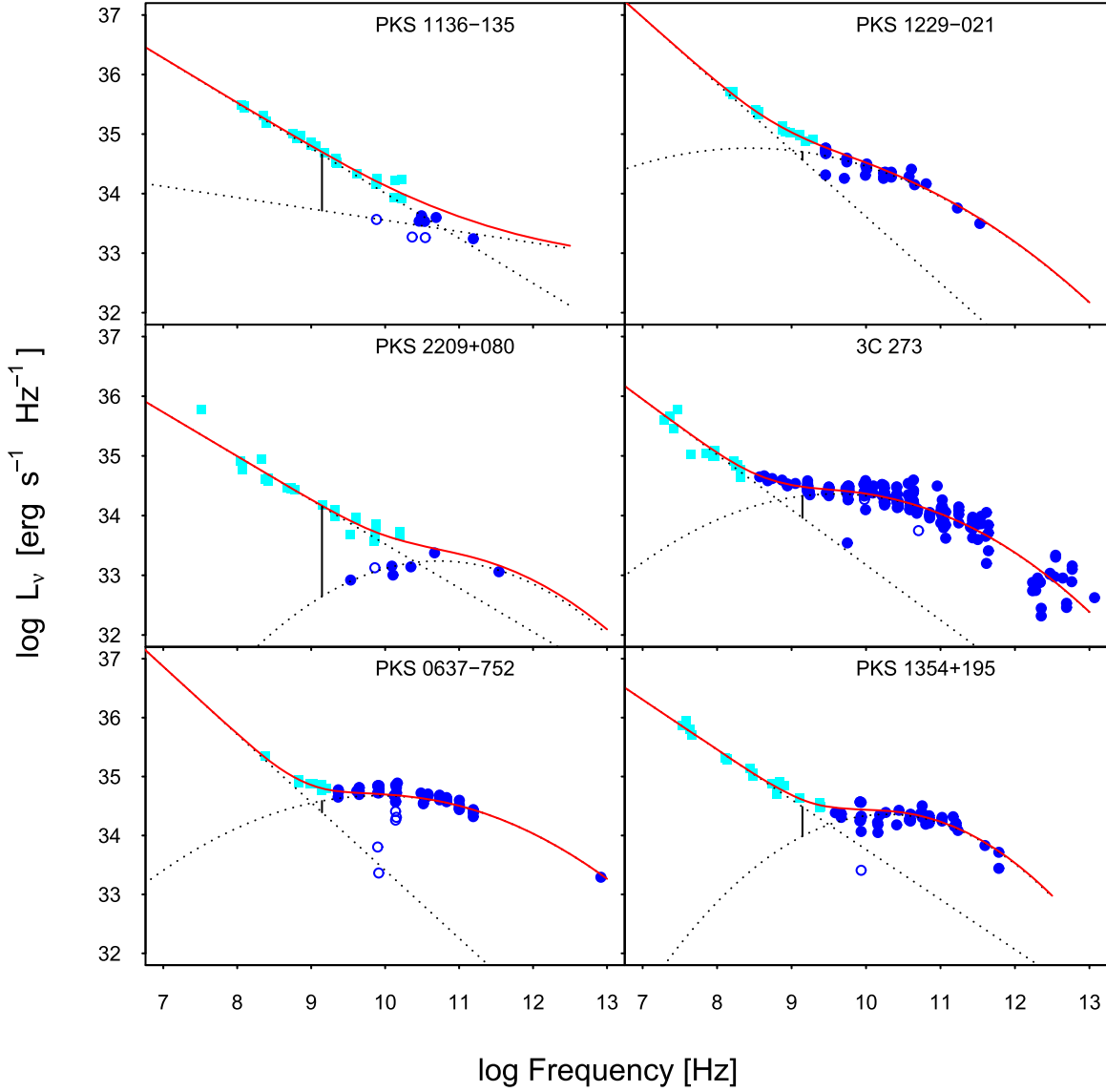
Figure 1. Low-frequency radio SEDs for the six sources where we have now ruled out IC/CMB as the X-ray emission mechanism. Data was obtained through the NED database, cyan squares represent extended lobe emission, blue circles represent core emission, and open circles represent data filtered out from the fitting. A power-law model was used to fit the lobe emission and a log parabola was used to fit the core emission, with dashed black lines showing each of the individual fits. The solid red line shows the total model fit adding both of these components for the radio spectrum. The solid black line connects the core and extended emission at 1.4 GHz, the ratio of which was used to determine the radio core dominance.

Table 1
Source Properties

(1) Source Name	(2) z	(3) kpc/$''$	(4) $\log M_{BH}/M_\odot$	(5) $\log L_{kin}$ (erg s^{-1})	(6) R_{CE}	(7) $\log \nu_{cross}$ (Hz)	(8) $\log \nu L_{\nu,peak}$ (erg s^{-1})	(9) $\log \nu_{peak}$ (Hz)	(10) Size (kpc)	(11) B_{eq} (10^{-4} G)
0637−752	0.650	6.75	9.41 (a)	45.9	0.19	9.01	46.3	13.4	164	1.15
1136−135	0.560	6.26	8.45 (b)	45.9	−0.72	10.7	45.4	14.1	92.9	0.470
1229−021	1.05	7.91	8.70 (b)	46.0	0.14	9.00	46.1	14.1	149	3.20
1354+195	0.720	7.03	9.44 (a)	45.8	−0.50	9.50	46.0	13.6	305	2.07
2209+080	0.480	5.80	⋯	45.5	−1.5	10.4	45.6	13.4	64.4	1.00
3C 273	0.160	2.65	8.91 (c)	45.5	0.37	8.82	45.9	14.4	63.6	1.00

Note. Size of the source is the projected size determined from hot spot to counter hot spot. (a), (b), and (c) black hole masses taken from Chen et al. (2015), Liu et al. (2006), and Kim et al. (2015), respectively.

"core" component as in Meyer et al. (2011) and shown in Figure 1. In this figure, we plot the lobe emission with cyan squares and the core emission with blue circles (data filtered out from the fitting is shown as open circles). The lobe and core emission were modeled with power-law and log-parabolic spectra, respectively, shown as the dotted lines, with the
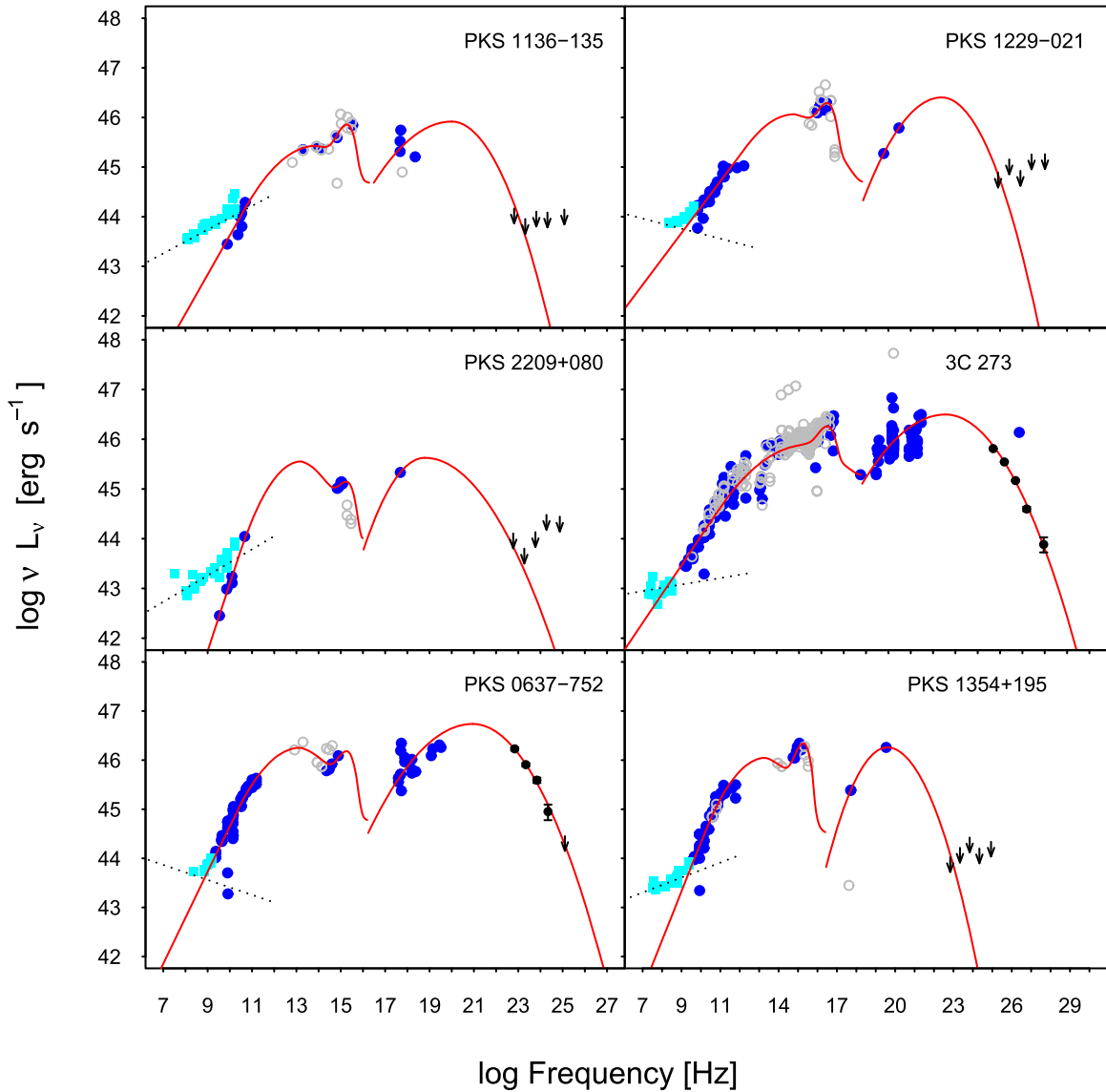
Figure 2. The SED for each source was fit with the parametric model from Meyer et al. (2011) shown in red, in order to estimate parameters for the synchrotron peak frequencies and luminosities. All data was obtained through NED, with the cyan squares representing the lobe spectrum, and the line of best fit shown as the dotted black line. Blue circles represent the rest of the data, and gray open circles represent the data that were filtered out and not used in the fitting. The *Fermi*/LAT data points are shown in black, with values taken from the 3FGL catalog for PKS 0637−752 and 3C 273, the rest being upper limits taken from the analysis done for this paper.

combined fit shown as a red line. In column 5, we give the kinetic jet power L_{kin}, where we have scaled from the 300 MHz radio luminosity of the lobes using the scaling of Cavagnolo et al. (2010). In column 6, we give the radio core dominance R_{CE}, where this is the logarithmic ratio of the core to extended (i.e., lobe) spectrum at 1.4 GHz. In column 7, we give the radio crossing frequency ν_{cross}, where this is the frequency that the core spectrum crosses with the lobe spectrum. Also following the methods described in Meyer et al. (2011), we made a simple phenomenological fit to the synchrotron spectrum in order to determine an approximate peak luminosity and frequency (L_{peak} and ν_{peak} respectively), which are given in columns 8 and 9 with the corresponding SED model fits shown in Figure 2. For the complete SEDs, we plot the lobe spectrum as cyan squares, *Fermi*/LAT data in black, the rest of the data with blue circles (data filtered out from the fitting is shown as gray circles), and the model fits as solid red lines. Finally, we give the projected size of the source and equipartition magnetic

field strength for the brightest X-ray knot, B_{eq}, in columns 10 and 11. It should be noted that all of these sources have high kinetic jet powers (see Figure 4 from Meyer et al. 2011) and black hole masses (see Figure 1 from Chiaberge & Marconi 2011) relative to other radio-loud AGN in general.

In this paper, we aim to test whether the high level of steady gamma-ray emission predicted under the IC/CMB model for the X-rays is seen. It is therefore essential that the precise level of the expected gamma-ray emission is known. As discussed in Georganopoulos et al. (2006), the X-ray to gamma-ray IC component has the same spectral shape as the radio-optical synchrotron spectrum, and the requirement to match the observed X-rays thus fixes the rest of the spectrum which peaks in the gamma-rays. It is thus critical that we compile the best possible multi-wavelength SEDs for the knots, from radio to X-rays. We describe here the archival and new data used to compile these SEDs for our four sources.

Table 2
VLA Archival Data

Source	Band (Config.)	Frequency (GHz)	Project	Date	TOS (m)	rms (μJy)	Beam (″)
1136−135	C (A)	4.860	AH938	2007 Jun 23	59	154	0.51 × 0.43
	X (B)	8.460	AC689	2008 Nov 03	447	111	1.01 × 0.74
	K (AB)	22.00	AC461	2002 May 27	107	123	0.25 × 0.15
1229−021	L (A)	1.505	AK95	1983 Oct 29	37	510	1.85 × 1.26
	C (A)	4.848	AK95	1983 Oct 29	18	305	0.61 × 0.40
	X (A)	8.350	AK353	1994 Mar 20	27	58	0.28 × 0.27
	U (B)	14.94	AK180	1987 Dec 12	114	72	0.59 × 0.42
1354+195	L (A)	1.425	AB920	1999 Jul 19	5	900	1.49 × 1.36
	C (B)	4.860	AB331B	1985 Apr 20	44	258	1.21 × 1.12
	X (B)	8.415	BL3	1993 Mar 08	33	135	1.21 × 0.77
2209+080	C (A)	4.86	AM723	2003 Aug 30	87	107	0.39 × 0.36
	U (B)	14.93	AM723	2002 Aug 20	96	90	0.44 × 0.41

2.2. VLA

As shown in Table 2, we used the deepest available archival *VLA* imaging of sufficient quality in bands L, C, X, and U (A or B configuration) to obtain a high-resolution image with the knots distinctly resolved. All sources were analyzed using CASA version 4.7.0. In all cases, either 3C 286 or 3C 48 was used as the flux density calibrator, and the source itself was used for gain calibration. We applied several rounds of self-calibration before generating the final image with clean. In Table 2, we list the source, band and configuration, central frequency of the observation, project code, date of observation, time on source (TOS) in minutes, rms of the final self-calibrated image in μJy, and size of the restoring beam in arcseconds.

2.3. VLBI

We searched for archival VLBI observations of our targets that can be used to measure the pc-scale jet proper motions. Three of the targets have no suitable archival data or were not observed with VLBI over multiple epochs. Only one target, PKS 1354+195, was observed four times (in 1997, 1999, 2002, and 2003) as part of the Monitoring Of Jets in AGNs with Very Long Baseline Array (VLBA) Experiments (MOJAVE) monitoring project (Lister et al. 2009, 2016), although no previous proper motion measurements were reported. We downloaded the fully-reduced fits images from the MOJAVE website and used the publicly available Wavelet Image Segmentation and Evaluation (WISE) code (Mertens & Lobanov 2015, 2016) to analyze the images for proper motions.

The WISE code comprises three main components. First, detection of structural information is performed using the segmented wavelet decomposition method. This algorithm provides a structural representation of astronomical images with good sensitivity for identifying compact and marginally resolved features and delivers a set of two-dimensional significant structural patterns (SSP), which are identified at each scale of the wavelet decomposition. Tracking of these SSP detected in multiple-epoch images is performed with a multi-scale cross-correlation algorithm. It combines structural information on different scales of the wavelet decomposition and provides a robust and reliable cross-identification of related SSP.

The images of PKS 1354+195 were taken with the VLBA at 2 cm (15 GHz) on 1997 August 18, 1999 July 19, 2002 August

Table 3
ALMA Observations

Source	Band	Cycle	Freq. (GHz)	TOS (s)	rms (μJy)	Beam (″)
1136−135	3	4	94.8	240	28	1.26 × 1.14
1229−021	3	4	97.5	66	171	0.76 × 0.53
	6	4	233	131	93	0.57 × 0.46
1354+195	3	4	97.5	72	224	0.76 × 0.53
	6	4	233	151	96	0.83 × 0.56
2209+080	3	3, 4	97.5	375	246	0.52 × 0.35
	6	4	233	454	161	0.61 × 0.46

12, and 2003 January 06. The images were centered on the core position and required no additional adjustment before analysis with WISE. The final reported proper motion values were obtained using a scale factor of six, though results were similar across a range of reasonable scale factors for the size of the knots in the jet. We only report those features detected in at least three of four epochs.

2.4. Atacama Large Millimeter/submillimeter Array (ALMA)

In Table 3, we list the *ALMA* data used in our analysis, where we give the observing band, cycle of the observations, effective frequency of the flux measurement, TOS, rms of the final image, and size of the restoring beam. *ALMA* observations were made of the first three targets as part of Cycle 3 and 4 programs 2015.1.00932.S and 2016.1.01481.S. Both programs included observations at band 3 and 6; however, only about 40% of the C-rated cycle 3 program was completed, and not all (A-rated) cycle 4 observations have been released. Forthcoming observations may improve on those presented in this paper. PKS 1136−135 was observed in band 3 by *ALMA* as a calibrator for a project unrelated to jets (program 2016.1.01250. S, PI: C. Peroux), and this data was kindly made available to us by the PI. For all sources, the data was first reduced using the provided scriptForPI.py script, which produces a calibrated measurement set appropriate for imaging with clean. The source scans were split off and several rounds of phase-only (non-cumulative) self-calibration were applied before a final (cumulative) round of amplitude and phase self-calibration. Clean was used in mfs mode, with nterms = 1 and Briggs weighting with robust = 0.5. The final rms measurements correspond to the primary-beam-corrected image, though we use the uncorrected images in the figures.
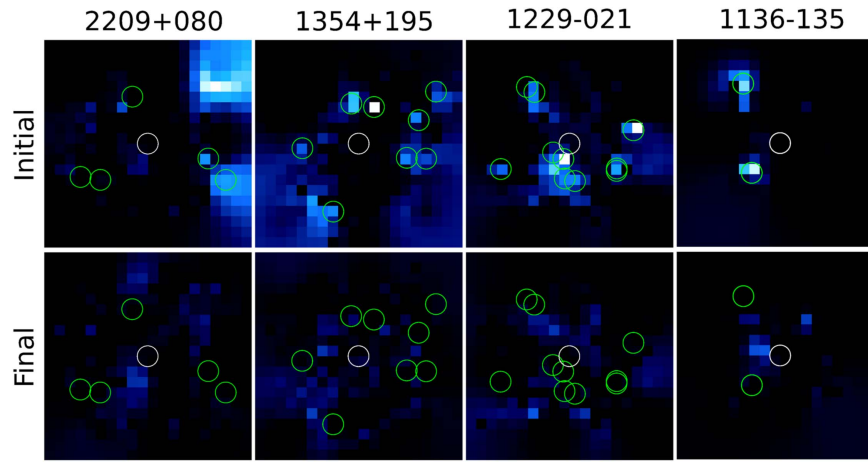
Figure 3. Initial and final Test Statistic (TS) residual maps for the region around each target, with final localized positions of all new non-3FGL sources shown as green circles and the source position as a white circle. Pixels are one square degree. The intensity scale ranges from a TS of 0 to 25 in all maps and from black to white, respectively.

In the case of 2209+080, we combined and imaged the somewhat lower-resolution cycle 4 data with the cycle 3 data, after core subtraction.

2.5. HST

Archival *HST* flux densities for the individual knots of 1354 +195 were taken from Sambruna et al. (2004), from Cara et al. (2013) for 1136-136, and from Tavecchio et al. (2007) for 1229–021.

PKS 2209+080 was observed as part of our *HST* program GO-13676 (PI: Meyer) and we present the results here for the first time. This source was observed for one orbit with the Wide Field Camera 3 (WFC3) in the near-infrared (IR) channel with filter F160W ($\lambda = 1.6\,\mu$m), and for two orbits with the Advanced Camera for Surveys Wide Field Camera (ACS/ WFC) with filter F606W ($\lambda = 6000\,$Å). In both cases, a dithering pattern was used to better sample the PSF, and the raw images were stacked using a routine similar to Astro-Drizzle, but better optimized for Astrometry. In particular, several dozen point sources in the optical image were used as a reference frame on which all images were aligned (final error on the registration is less than 1 mas). This allowed us to precisely align the optical and IR images, which allows for better identification of common features in both. The final pixel scale in both images is 25 mas.

We did not attempt a galaxy subtraction, as it has a very irregular profile and models produced by `iraf` tasks `ellipse` and `bmodel` left large residual errors. We measured flux densities using contours around each knot, estimating the background by moving the same contour to 6–8 positions at the same radius from the galaxy center. The mean background value was subtracted from the initial flux density measurement, and errors are taken to be $\sqrt{2}$ times the standard deviation of the background flux densities. The flux densities were measured using the viewer utility of the `CASA` package.

2.6. Fermi

By design, each of the four targets was not a member of the 3FGL 4 year point source catalog for the *Fermi*/LAT. We first checked if any of the sources would be detected using data for the entire time range since the launch of *Fermi* in 2008 (over eight years). *Fermi*/LAT event and spacecraft data were

extracted using a 10° ROI, an energy cut of 100 MeV– 100 GeV, a zenith angle cut of 90°, and the recommended event class and type for point source analysis for all sources except PKS 1136–135, where a 7° ROI was used. The time cuts included all available *Fermi* data at the time of analysis with corresponding mission elapse time (MET) ranges of 239557417 to 510106834 for PKS 1136–135, 239557417 to 501427132 for PKS 1229–021, 239557417 to 239557417 for PKS 1354+195, and 239557417 to 503840003 for PKS 2209 +080. Following the standard methodology for *Fermi*/LAT binned likelihood analysis, a binned counts map was made with 30 logarithmically spaced energy bins and 0.2 degree spatial bins in all cases. Initial spatial and spectral model files for each source were constructed with sources up to 10° outside the ROI, using the publicly available `make3FGLxml.py` script. This populates the model file with point and extended sources from the *Fermi*/LAT 3FGL catalog and an extended source catalog, respectively. Additionally, the current galactic diffuse emission model, `gll_iem_v06.fits`, and recommended isotropic diffuse emission model for point source analysis, `iso_P8R2_SOURCE_V6_v06.txt`, were used for the ana- lyses. The livetime cubes were computed using 0.025 steps in $\cos(\theta)$ (where θ is the inclination with respect to the LAT's z-axis) and 1° spatial binning. All-sky exposure maps were then computed using the same energy binning as the counts maps. After obtaining converged fits following the maximum like- lihood optimizations with the initial model, Test Statistic (TS) residuals maps with 1° spatial binning were created to find new point sources not accounted for in the 3FGL catalog, following the procedure outlined in Meyer et al. (2015). The TS is defined as twice the logarithmic ratio of the maximum likelihood calculated with an additional point source at the specified location to the maximum likelihood without an additional source, and can be taken as roughly the significance squared. In Figure 3, we show the TS residual maps created before and after adding the new sources not accounted for in the 3FGL catalog. The new source positions are shown with green circles, and the sources we obtained upper limits for this paper are shown with white circles.

In locations where TS residual values were greater than 10, we added point sources with power-law spectra to the model files and optimized their positions and spectral parameters. After obtaining converged maximum likelihood fits for the

Table 4
1136−135 Broadband Jet Knot Emission

Feature	$F_{4.8\ GHz}$ (mJy)	$F_{9.4\ GHz}$ (mJy)	$F_{22\ GHz}$ (mJy)	$F_{5.8\ \mu m}$ (μJy)	$F_{3.6\ \mu m}$ (μJy)	$F_{815\ nm}$ (μJy)	$F_{626\ nm}$ (μJy)	$F_{555\ nm}$ (μJy)	$F_{475\ nm}$ (μJy)	$F_{1\ keV}$ (nJy)	α_r	Distance from Core (″)
α	2.90	1.50	0.500	⋯	⋯	337	330	358	362	1.90	0.59	2.7
A	3.85	2.00	0.650	⋯	⋯	237	208	212	231	1.70	0.60	4.9
B	8.00	3.20	⋯	4.80	3.80	535	396	365	320	3.50	0.61	6.8
C	30.8	9.20	⋯	⋯	⋯	342	⋯	148	⋯	1.80	0.80	7.8
D	59.8	11.9	⋯	⋯	⋯	390	191	140	⋯	1.00	1.1	8.6
E	114	26.4	⋯	⋯	⋯	161	⋯	130	⋯	0.700	0.97	9.3

Table 5
1229−021 Broadband Jet Knot Emission

Feature	$F_{1.4\ GHz}$ (mJy)	$F_{4.8\ GHz}$ (mJy)	$F_{8.4\ GHz}$ (mJy)	$F_{15\ GHz}$ (mJy)	$F_{97\ GHz}$ (mJy)	$F_{233\ GHz}$ (mJy)	$F_{692\ nm}$ (μJy)	$F_{1\ keV}$ (nJy)	α_r	Distance from Core (″)
A	⋯	21.7	20.0	10.4	⋯	⋯	⋯	⋯	0.66	0.70
BCD	274	100	65.4	42.2	10.4	4.50	0.470	8.50	0.80	1.9

Table 6
1354+195 Broadband Jet Knot Emission

Feature	$F_{1.4\ GHz}$ (mJy)	$F_{4.8\ GHz}$ (mJy)	$F_{8.4\ GHz}$ (mJy)	$F_{97\ GHz}$ (mJy)	$F_{233\ GHz}$ (mJy)	$F_{814\ nm}$ (μJy)	$F_{586\ nm}$ (μJy)	$F_{475\ nm}$ (μJy)	$F_{1\ keV}$ (nJy)	α_r	Distance from Core (″)
A	131	49.2	32.0	5.20	3.50	0.530	0.300	0.195	16.1[a]	0.77	1.7
B	30.8	14.2	7.60	1.55	0.477	0.0770	0.0400	0.0470	0.700	0.79	4.0

Note.
[a] This flux density is in dispute, and more appropriately may be a non-detection with an upper limit of 0.39 nJy (Harris et al. 2017).

Table 7
2209+080 Broadband Jet Knot Emission

Feature	$F_{4.8\ GHz}$ (mJy)	$F_{15\ GHz}$ (mJy)	$F_{233\ GHz}$ (mJy)	$F_{1.6\ \mu m}$ (μJy)	$F_{600\ nm}$ (μJy)	$F_{1\ keV}$ (nJy)	α_r	Distance from Core (″)
A	30.0	15.1	2.22	4.40	2.41	⋯	0.78	0.52
B	21.0	12.2	2.18	1.64	0.570	⋯	0.60	1.3
C	24.0	13.1	2.11	0.950	0.260	⋯	0.64	2.0
D	8.20	5.00	1.15	0.170	⋯	⋯	0.52	3.2
E	29.7	16.4	2.02	1.58	0.430	4.76	0.71	4.7

updated model file, our target source of interest was added to the model file with a fixed photon index (1.93 for PKS 1136–135, 2.39 for PKS 1229–021, 1.94 for PKS 1354 +195, and 1.65 for PKS 2209+080). These photon indices were derived from the implied gamma-ray index of the IC/ CMB model. After this, the upper limits in the five *Fermi* energy bands of 100 MeV–300 MeV, 300 MeV–1 GeV, 1 GeV–3 GeV, 3 GeV–10 GeV, and 10 GeV–100 GeV were computed by running the analysis tools separately on each data set with the appropriate energy range data cuts.

3. Results

In Tables 4–7, we present the flux densities from radio through X-ray wavelengths of each identified knot of sources 1136–135, 1229–021, 1354+195, and 2209+080, respectively, with the corresponding radio spectral index and distance of the knot from the core. The radio spectral index, α_r, is defined using the convention $F_\nu \propto \nu^{-\alpha_r}$. In Figure 4, we show the broadband SEDs for (typically) the most X-ray prominent knots in each source. In the case of PKS 1354+195, we also

show the total X-ray flux density of the jet after knot A, and in PKS 1229–021, we show the combined flux density of knots B, C, and D, which could not be separately resolved in all imaging.

In Figure 4, observed flux densities are plotted (in νF_ν) as blue and green squares with thin solid black lines showing the synchrotron model fits to the radio-optical data. In all cases, the radio-optical spectrum is modeled as a power law with scaled exponential cutoff, as described in the Appendix. The thicker black lines are the IC/CMB model fits to the X-ray flux densities. The IC/CMB model curves are copies of the synchrotron curves, shifted in frequency and luminosity by an amount proportional to δ/B and $(\delta/B)^2$, respectively, where δ/B is the only free parameter in the shift, set by the requirement to reproduce the observed X-ray flux density. The equations governing the shift are given in the Appendix (see also Georganopoulos et al. 2006).[4] The 95% *Fermi* upper

---

[4] B is the magnetic field strength of the emitting region and δ is the Doppler factor given by $\delta = \Gamma/(1 - \beta \cos\theta)$. Here, Γ is the bulk Lorentz factor, β is the bulk speed flow scaled by c, and θ is the jet angle to the line of sight.
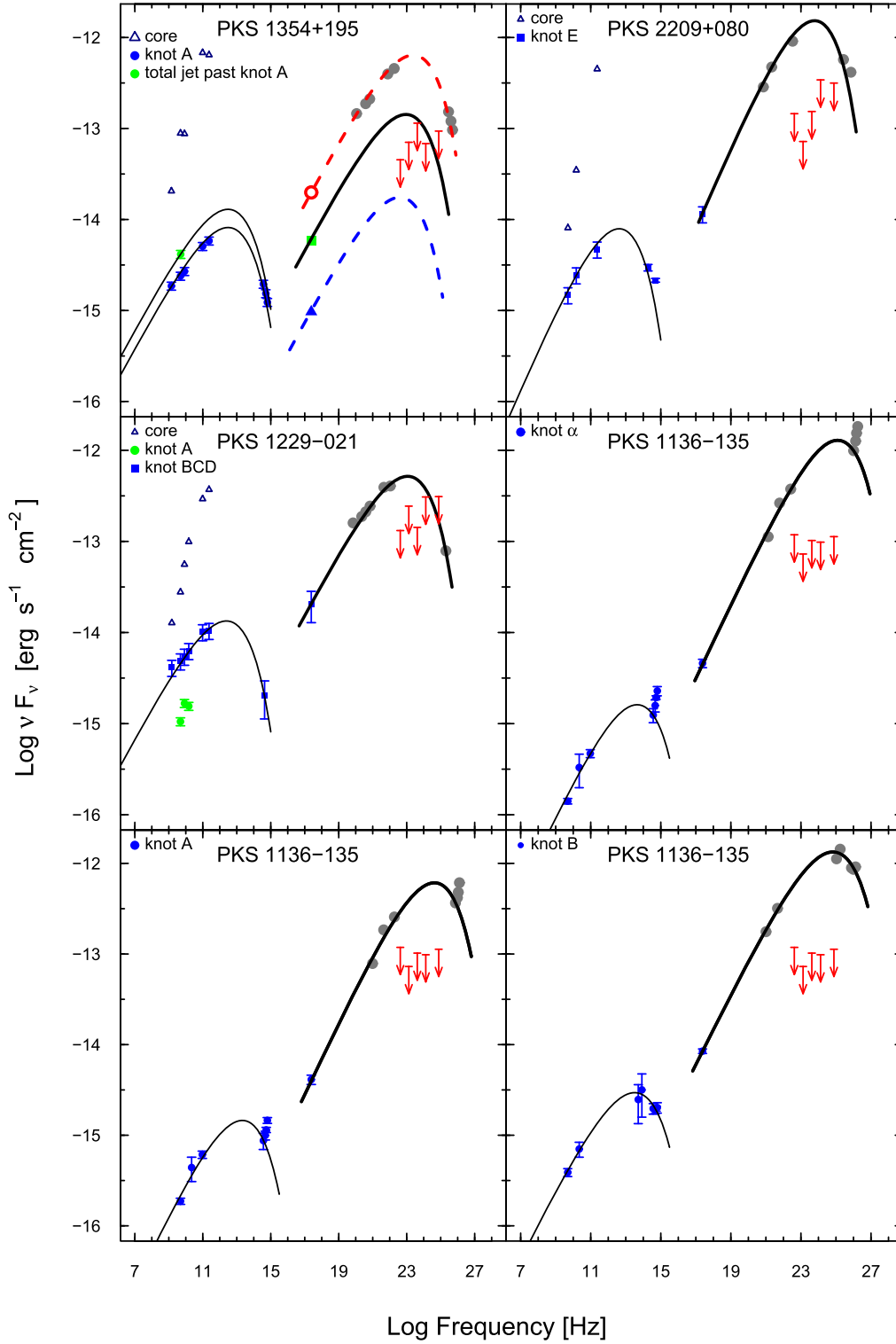
Figure 4. SEDs for the jet knots of PKS 1354+195 (top left), PKS 2209+080 (top right), PKS 1229–021 (middle-left), and PKS 1136–135 (middle right and bottom row). Thin black curves show phenomenological synchrotron model fits; thick black curves show the corresponding IC/CMB model curves, normalized to match the X-ray flux densities. The gray points represent where the radio through optical data points would lie on the IC/CMB model curves after shifting in frequency and luminosity by the appropriate amount. The 95% *Fermi* upper limits are shown in red. For PKS 1229–021, blue data points correspond to the combined data for knots B, C, and D. The green data points for PKS 1354+195 correspond to the combined data for all knots past knot A, with the X-ray point being a lower limit and shown as a square (all data for PKS 1354+195 except the *Fermi* limits and the radio/*ALMA* data of knot A are taken from Sambruna et al. 2004). The red open circle and red dashed line for PKS 1354+195 show the original 8.2 nJy X-ray flux density for knot A reported by Sambruna et al. (2002), with the corresponding IC/CMB model fit. The blue triangle for PKS 1354+195 shows the 0.39 nJy upper limit for the X-ray flux density of knot A obtained by Harris et al. (2017), with the corresponding IC/CMB model curve shown as a blue dashed line. The thick black line in the PKS 1354+195 SED is the IC/CMB model curve for the total jet past knot A. The X-ray and optical data for PKS 1229–021 are taken from Tavecchio et al. (2007); the X-ray data for PKS 2209+080 are taken from Jorstad & Marscher (2006), and the X-ray, infrared, and optical data for PKS 1136–135 are taken from Cara et al. (2013).

Table 8
Results of the *Fermi* Data Analysis

(1) Source Name	(2) Feature	(3) Band	(4) E_1 (GeV)	(5) E_2 (GeV)	(6) log freq (Hz)	(7) Predicted $\nu F_{\nu,\mathrm{IC/CMB}}$ (erg s^{-1} cm^{-2})	(8) 95% νF_ν Limit (erg s^{-1} cm^{-2})	(9) % Ruled Out	(10) σ	(11) δ Limit
1136–135	B	1	0.1	0.3	22.6	5.7×10^{-13}	1.18×10^{-13}	99.996	3.94	5.4
		2	0.3	1	23.1	7.7×10^{-13}	7.27×10^{-14}	>99.99999	6.29	⋯
		3	1	3	23.6	9.9×10^{-13}	1.02×10^{-13}	>99.99999	7.58	⋯
		4	3	10	24.1	1.2×10^{-12}	9.81×10^{-14}	>99.99999	8.13	⋯
		5	10	100	24.7	1.3×10^{-12}	1.13×10^{-13}	>99.99999	6.01	⋯
1229–021	BCD[a]	1	0.1	0.3	22.6	4.9×10^{-13}	1.32×10^{-13}	99.97	3.40	8.0
		2	0.3	1	23.1	5.2×10^{-13}	2.44×10^{-13}	99.91	3.11	⋯
		3	1	3	23.6	4.8×10^{-13}	1.43×10^{-13}	99.998	4.07	⋯
		4	3	10	24.1	3.9×10^{-13}	3.07×10^{-13}	97.6	1.98	⋯
		5	10	100	24.7	2.1×10^{-13}	3.10×10^{-13}	85.8	1.07	⋯
1354+195	jet[b]	1	0.1	0.3	22.6	1.4×10^{-13}	4.53×10^{-14}	99.83	2.92	6.0
		2	0.3	1	23.1	1.4×10^{-13}	7.05×10^{-14}	99.27	2.44	⋯
		3	1	3	23.6	1.3×10^{-13}	1.14×10^{-13}	96.60	1.83	⋯
		4	3	10	24.1	9.9×10^{-14}	6.83×10^{-14}	97.98	2.05	⋯
		5	10	100	24.7	5.1×10^{-14}	9.36×10^{-14}	88.49	1.20	⋯
2209+080	E	1	0.1	0.3	22.6	1.1×10^{-12}	1.45×10^{-13}	>99.99999	5.23	8.6
		2	0.3	1	23.1	1.3×10^{-12}	7.19×10^{-14}	>99.99999	>8.2	⋯
		3	1	3	23.6	1.5×10^{-12}	1.54×10^{-13}	>99.99999	>8.2	⋯
		4	3	10	24.1	1.5×10^{-12}	3.42×10^{-13}	>99.99999	7.87	⋯
		5	10	100	24.7	1.1×10^{-12}	3.15×10^{-13}	99.999	4.34	⋯

Notes.
[a] Knot BCD includes the combined data from knots B, C, and D.
[b] Data was combined for the whole jet past knot A.

limits are shown as red arrows. As can be seen, the *Fermi* upper limits are well below the IC/CMB model curves in each SED and we can reject the IC/CMB model as the X-ray emission mechanism for each source.

The results of the *Fermi* analyses, corresponding to the plotted limits, are given in Table 8. For all five *Fermi* bands, we give the minimum and maximum energy in columns 4 and 5. The logarithmic mean frequency of each band is given in column 6, corresponding to the frequency of the predicted IC/CMB flux densities (column 7) and the observed 95% upper limits (column 8). In columns 9 and 10, we give the confidence with which we can rule out the IC/CMB model for each X-ray knot as a percentage and sigma level. Finally, in column 11, we derive and list the upper limit on the Doppler factor, assuming an equipartition magnetic field. Combining the individual band results using the inverse normal method, we find the IC/CMB model is ruled out at the 14.3σ, 6.1σ, 4.7σ, and $>15.2\sigma$-levels for PKS 1136–135, PKS 1229–021, PKS 1354+195, and PKS 2209+080, respectively. Additionally, in Figure 4 we use gray closed circles to plot where the observed synchrotron data points would lie in the shifted IC/CMB spectrum. This was done to emphasize the point that the *Fermi* upper limits directly violate the IC/CMB predicted flux densities from observed portions of the synchrotron spectrum.

Radio, sub-mm, optical (for 2209+080), and X-ray images of each source in this study are shown in Figures 5–8, along with the knot identifications used in this paper (which in some cases vary from previous usage in the literature). In all four cases, there is no detectable counter-jet at any wavelengths, but we do detect the counter-hot spots in the radio (and in some cases with *ALMA*). We now discuss the observations of each source in turn.

3.1. PKS 1136–135

PKS 1136–135 is a powerful FR II source previously observed by Sambruna et al. (2006) with *Chandra* and *HST*, where they modeled the X-ray emission with the IC/CMB model. Our multi-wavelength images are shown in Figure 5, where we see a straight and knotty radio jet, with knots brighter toward the hot spot in the radio. Knots B, C, D, and E are not separately resolved by *ALMA,* so we do not include *ALMA* flux densities for the jet SED. In Figure 4, we show the SED of knots α, A, and B, where our gamma-ray upper limits are well below the extrapolated IC/CMB emission in all three cases. Our limits were not deep enough to rule out IC/CMB for the last three knots, which had low IC/CMB predicted gamma-ray flux densities. In knots α and A, there is an upturn in the SED at 815 nm that lies above a single power-law fit for the synchrotron spectrum. Fitting these UV-upturns with an IC/CMB model is problematic because this would require very high levels of X-ray emission not observed by *Chandra*. Therefore, these UV-upturns imply a second higher-energy electron distribution also responsible for the X-ray emission, similar to that seen in 3C 273. Cara et al. (2013) showed, with *HST* polarimetry, that all of the jet knots had fractional polarization measures in excess of 30% (except knots α and B, where they found 2σ upper limits of 15% and 14% respectively). For the cases where the UV emission is clearly part of the second spectral component, these high degrees of polarization provide strong evidence against the IC/CMB model. However, our gamma-ray upper limits provide another independent line of evidence ruling out the IC/CMB model in knot A, while our upper limits show that the IC/CMB model is ruled out for knots α and B, which did not have high degrees of polarization. Fitting the UV data with an IC/CMB model for knots α and A would also predict much higher X-ray flux
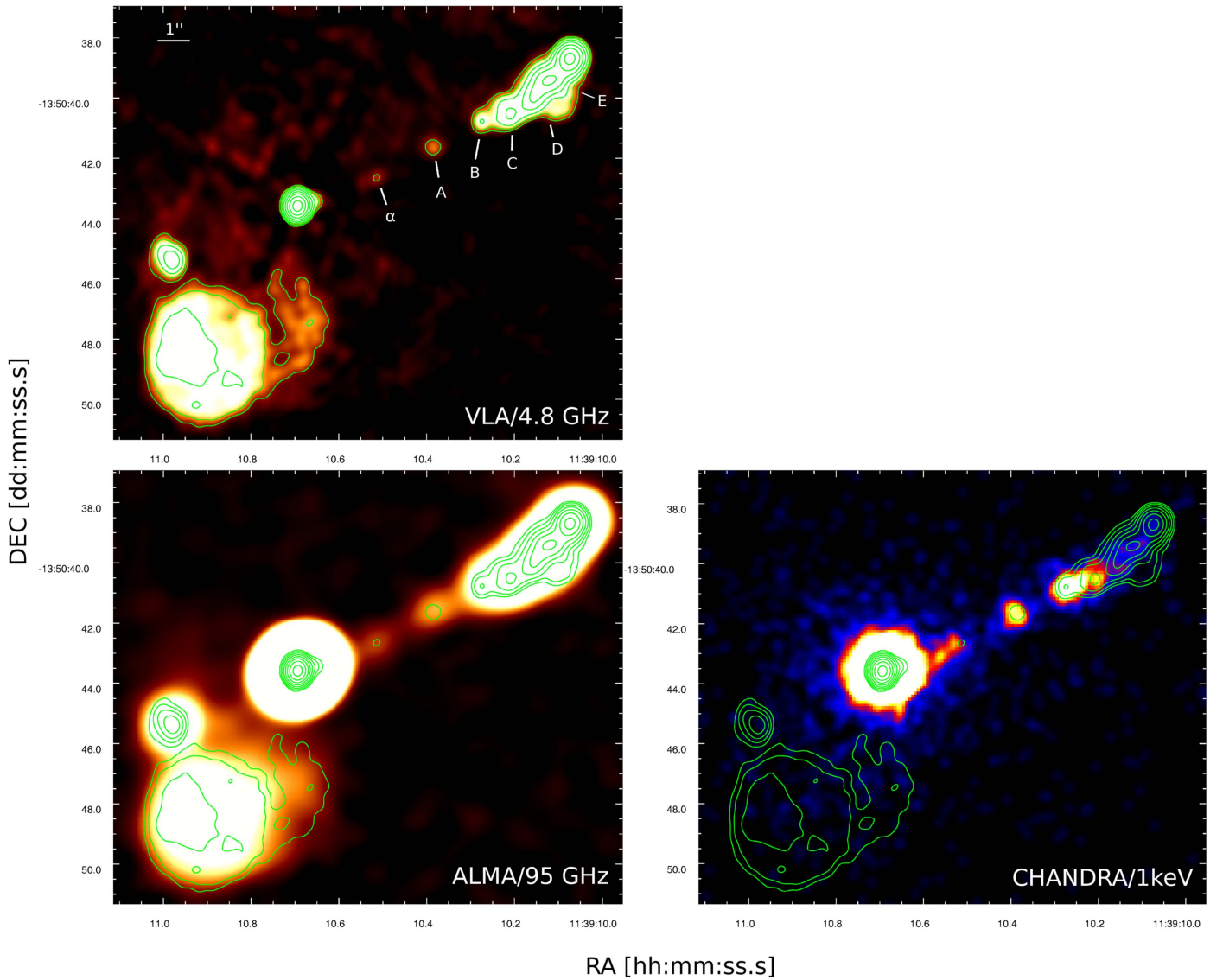
Figure 5. Multi-wavelength images of PKS 1136–135, where 4.8 GHz *VLA* contours were used for all images. Contours are spaced by a factor of 2, with a base level of 1.5 mJy. The top left panel is a 4.8 GHz *VLA* image, the bottom left panel is *ALMA* band 3, and the bottom right panel is a 1 keV *Chandra* image. The *Chandra* image is smoothed with a Gaussian with a radius of three pixels.

densities than observed, though the UV spectrum is also much harder than would be consistent with an IC/CMB model fit.

3.2. PKS 1229–021

PKS 1229–021 was previously observed and modeled as an IC/CMB X-ray jet by Tavecchio et al. (2007), where we use their reported *HST* and *Chandra* densities in our SED (Figure 4). The radio images shown in Figure 6 show four well-defined cannonball-like knots downstream of the core. Interestingly, similar periodic knot structures are seen in all six of the jets discussed in this paper. As shown in Figure 6, knots B, C, and D are not separately resolved by *ALMA* and *Chandra*. Thus, we combined the data for these knots, labeled as knot BCD. Past this combined feature, we see the jet is considerably bent, implying a change of jet direction. Our *ALMA* images (which are core-subtracted) are focused on the jet in order to emphasize the knot structure. We found the western hot spot was only detected by *ALMA* in band 3, but not

in band 6. The *HST* data presented in Tavecchio et al. (2007) shows that only the combined knot BCD was detected in the *HST* imaging, while knot A is not detected. With only one optical data point, the synchrotron SEDs for both of these features are not as well-constrained as for our other sources. Therefore, we believe that this source would be a good candidate for follow-up *HST* observations in order to further constrain the SED.

3.3. PKS 1354+195

This source is shown in Figure 7, where the radio observations show a straight jet with detailed hot spot structure for the northern hot spot. The *VLA* and *ALMA* observations again show a well-defined cannonball-like knot structure for knots A and B. This jet was previously observed and modeled as an IC/CMB X-ray jet by Sambruna et al. (2002, 2004), so we use their reported *HST* and *Chandra* flux densities from the 2004 publication. Initially, we focused on knot A, which was reported as brightest in the
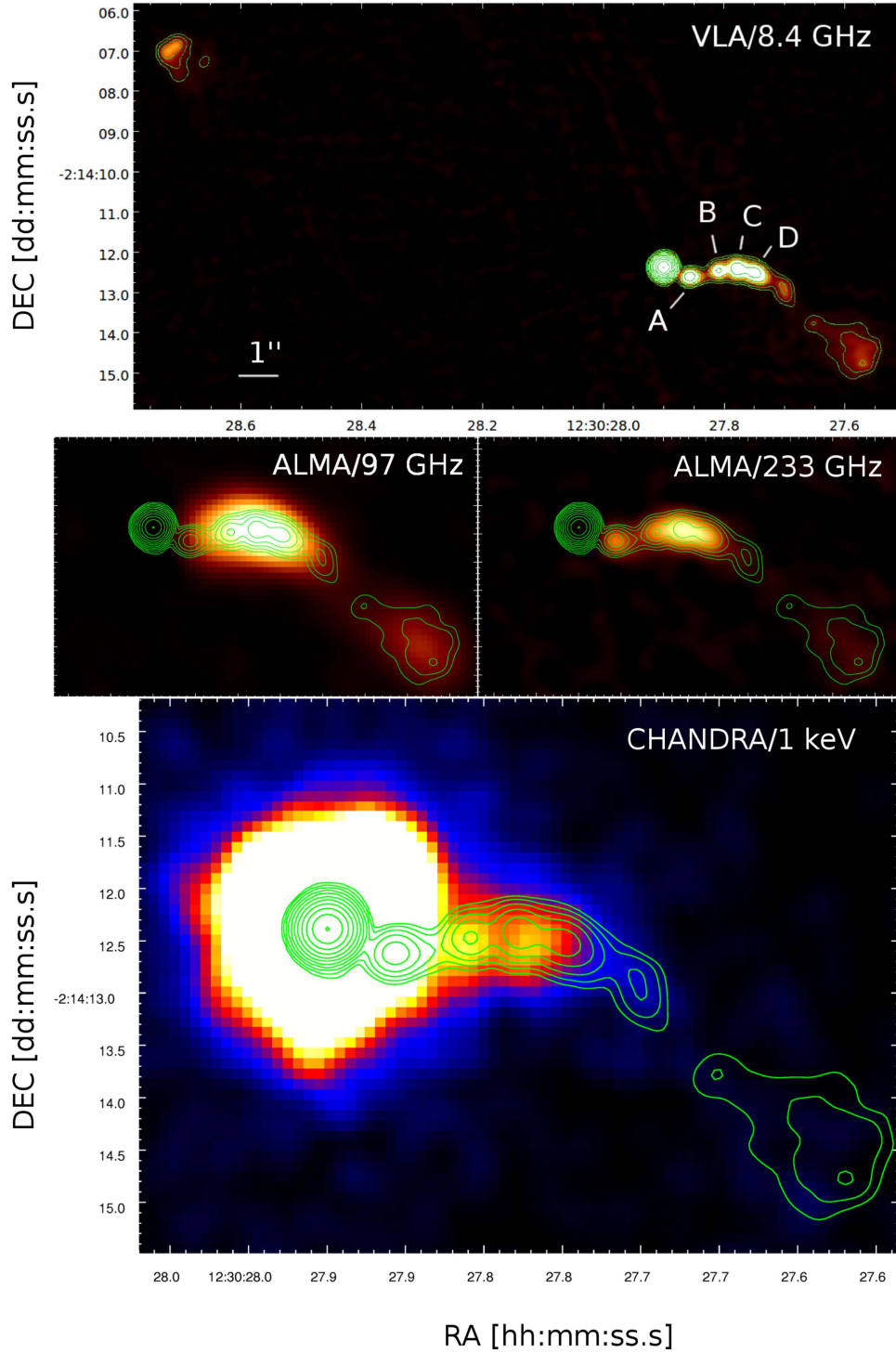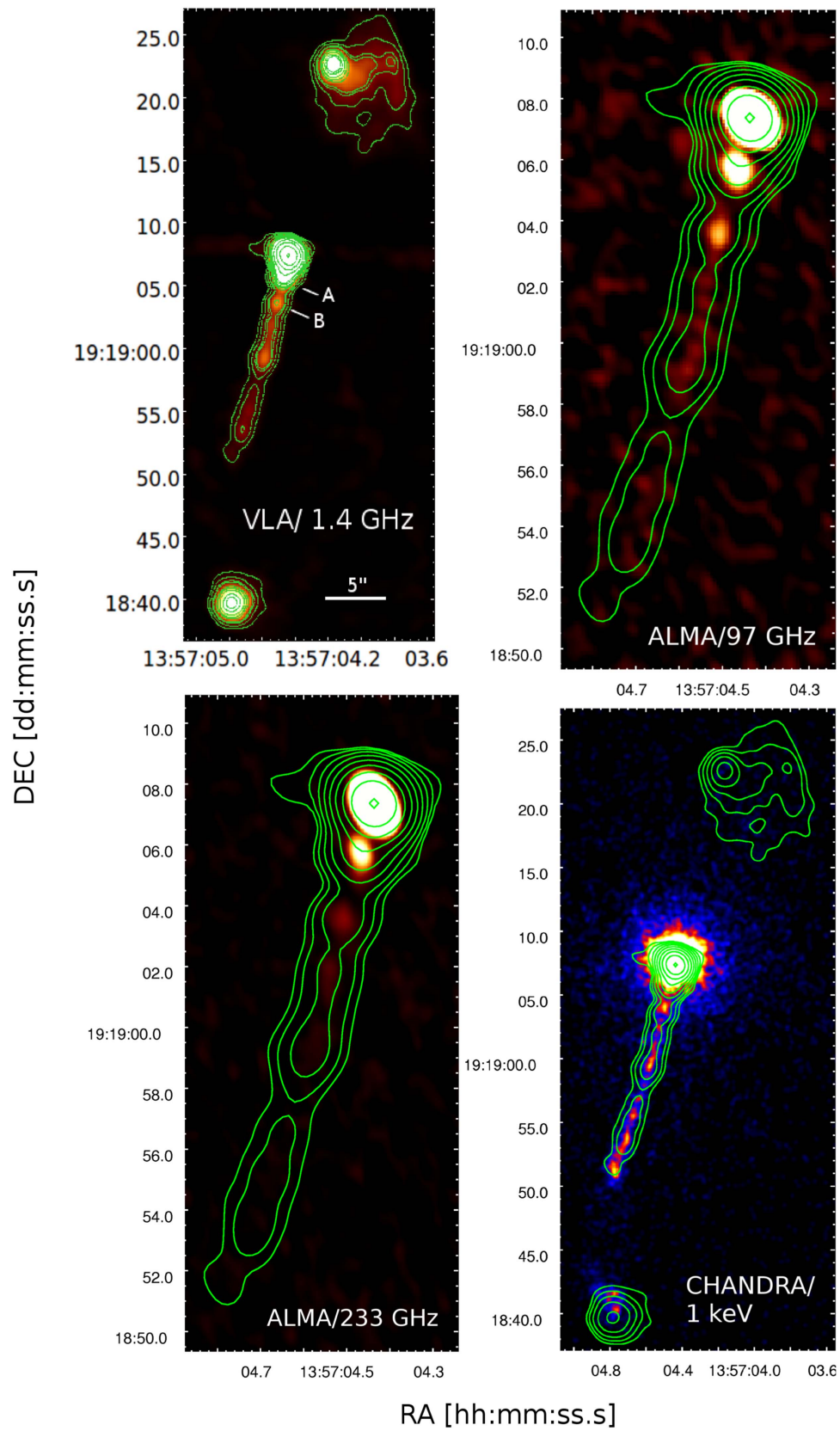
Figure 6. Multi-wavelength images for PKS 1229–021 where 8.4 GHz *VLA* contours were used for all images. The contours are spaced by factors of 2, with a base level of 0.63 mJy. The upper panel is an 8.4 GHz *VLA* image, the middle panels are *ALMA* band 3 and 6 images, and the lower panel is a *Chandra* 1 keV image. The *Chandra* image is smoothed with a Gaussian with a radius of three pixels. The *ALMA* images are focused on the jet and hot spot, and are core-subtracted.

X-rays. This knot is approximately 2″ from the core and initially reported in Sambruna et al. (2002) to have a flux density of 8.2 nJy (corresponding to about 135 counts) and later revised to 16.1 nJy in Sambruna et al. (2004). However, deeper *Chandra* observations of PKS 1354+195 suggest that knot A is in fact not detectable separate from the bright quasar core, with an upper limit of <0.39 nJy, after taking into account careful modeling of the PSF from the core (Harris et al. 2017). We plot the 8.2 nJy

Chandra flux density in Figure 4 as a red open circle. While this flux density implies that the IC/CMB model is ruled out at a very high level of significance (see red dashed line), the much lower revised flux density limit (blue triangle and dashed line) does not. In light of this revision, we also examined the newer *Chandra* observations and can confirm that we do not find a significant excess of counts at the position of knot A in any of the later observations, suggesting that the apparent excess in the early

Figure 7. Multi-wavelength images of PKS 1354+195 where 1.4 GHz *VLA* contours were used for all images. The contours are spaced by factors of 2, with a base level of 5.2 mJy. The upper left panel is a 1.4 GHz *VLA* image, the upper right panel is *ALMA* band 3, the lower left panel is *ALMA* band 6, and the lower right panel is a 1 keV *Chandra* image. *ALMA* images are focused on the jet to show the knot structure. The *Chandra* image is smoothed with a Gaussian with a radius of three pixels.
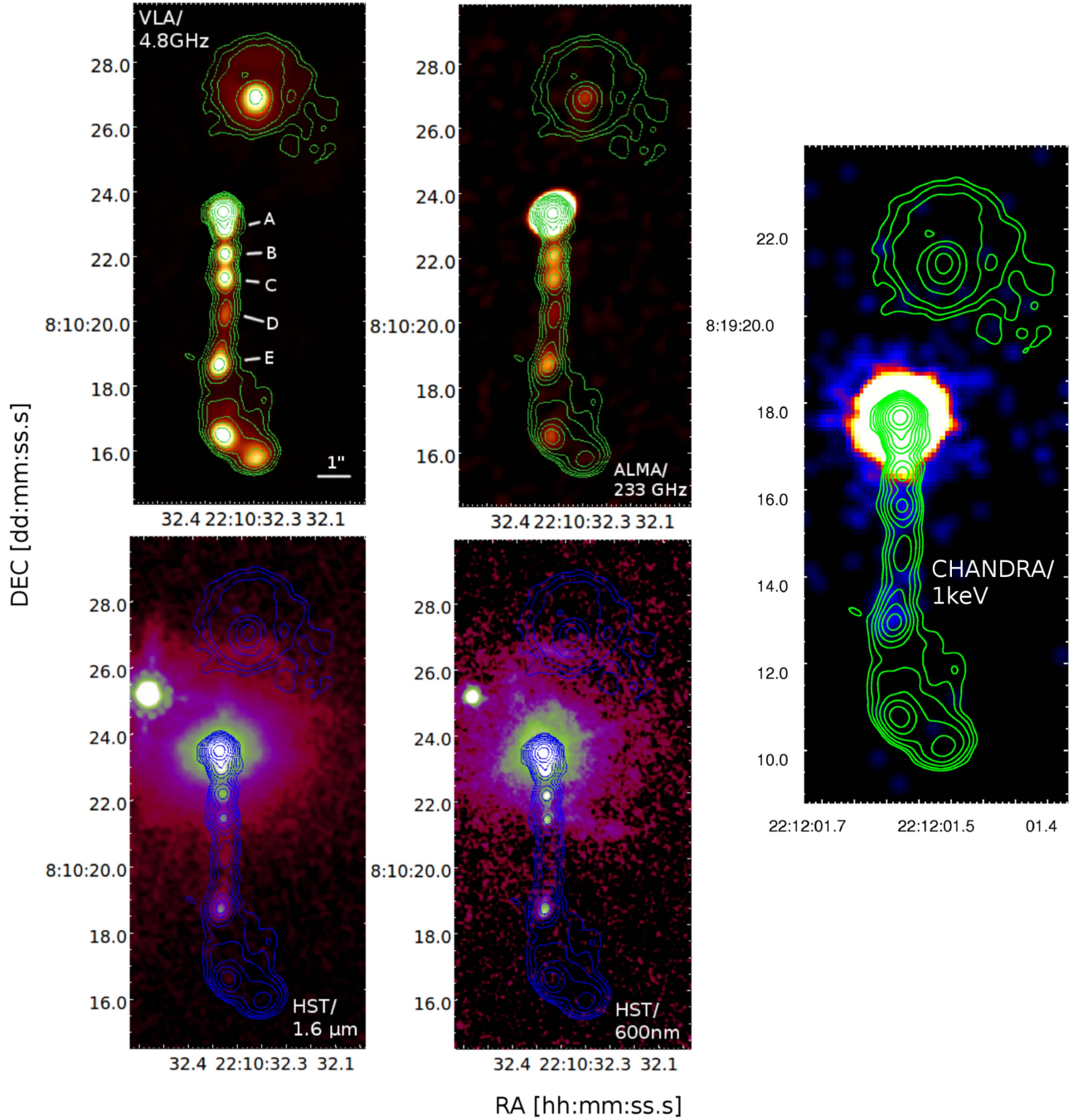
Figure 8. Multi-wavelength images of PKS 2209+080 with 4.8 GHz *VLA* contours for all images. The contours are spaced by factors of 2, with a base level of 56 mJy. The upper left panel is a 4.8 GHz *VLA* image, the upper middle panel is an *ALMA* band 6 image, the right panel is a 1 keV *Chandra* image, and the lower left images are *HST* 1.6 μm and 600 nm. The 600 nm image is smoothed with a Gaussian with a radius of three pixels.

observation (*Chandra* Observation ID #2104) was a statistical fluctuation. The jet of PKS 1354+195 is quite straight up to just before the hotspot, suggesting no major bends in or out of our line of sight. If knot A has the same radio to X-ray ratio as knot B, we would expect an X-ray flux density of about 2.4 nJy. However, the very bright core makes it difficult to conclude much from knot A. Turning to the remaining knots in the jet, and assuming *some* level of X-ray flux density from knot A, we produce the *lower limit* X-ray flux density shown as a green square in the SED figure with a value of 2.4 nJy. Note this is

approximately the same X-ray flux density calculated for knot A, assuming the same radio to X-ray ratio as knot B. Using this and the spectral shape determined by knots A and B together from radio-optical, we see that the IC/CMB model is still ruled out, though the case is not as strong as in the other sources presented in this paper.

Note that, in Table 8, the predicted IC/CMB level, the 95% upper limits, and the corresponding confidence and limits on δ all correspond to the more reliable estimates derived from the knots excluding knot A.
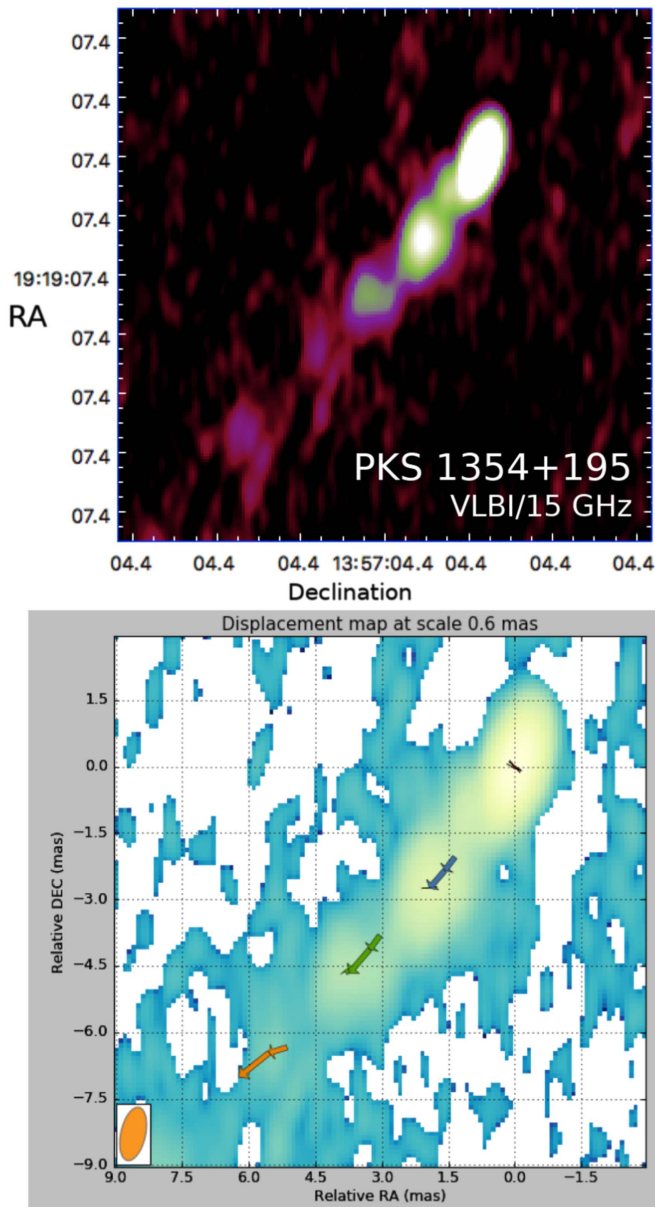
13

Figure 9. Top: parsec-scale jet of PKS 1354+195 in 2002 taken with VLBA at 15 GHz (Lister et al. 2009). Below: results of the WISE proper motion analysis of the four available VLBA epochs, with arrows showing the motions from epoch-to-epoch for three components in the jet (the core is stationary and consistent with no motion as expected).

3.3.1. VLBI Proper Motions

PKS 1354+195 was the only source for which archival VLBA data were available for a proper motion analysis. The results of the WISE analysis reveal three moving features in the jet. We show the pc-scale jet in the 2002 epoch and the results of the WISE feature tracking in Figure 9. Ordered by distance from the core, the moving features show angular motions of 0.17 ± 0.01, 0.21 ± 0.01, and 0.26 ± 0.20 mas yr^{-1}. At the scale of 7.32 parsecs per mas, this corresponds to a apparent proper motions of $4.00 \pm 0.24c$, $4.95 \pm 0.24c$ and $6.1 \pm 4.7c$. The last of these components is only detected in the last three images and has a rather large error bar, but the other two components are secure detections in all four epochs. We re-analyzed the data using a variety of possible scales for the components and found results very consistent with the above.

3.4. PKS 2209+080

PKS 2209+080 was previously observed and modeled as an IC/CMB X-ray jet by Jorstad & Marscher (2006), where we used their X-ray flux density in our SED. As shown in Figure 8, PKS 2209+080 has a very knotty and straight jet, with the southern hot spot showing two resolved components. Our *ALMA* and *HST* observations resolve all of the identified radio knots. As can be seen in both *HST* images, the host galaxy has an irregular tail structure that is suggestive of a possible recent merger. Only the southern hot spot is detected in the infrared as shown in the lower-middle panel of Figure 8. The only knot reported to show X-ray emission by Jorstad & Marscher (2006) was knot E. In Figure 10, we show the SEDs of knots A through D, which are upstream of knot E, with data shown as squares and synchrotron model fits as solid lines. In knots A through C, there is an upturn in the SED at 600 nm, which lies above a single power-law fit for the synchrotron spectrum. Similar to the cases of PKS 1136–135 and 3C 273, fitting these UV-upturns with an IC/CMB model would require X-ray flux densities much higher than those observed by *Chandra*.

4. Discussion

4.1. IC/CMB Now Ruled Out for Six Sources

The IC/CMB model for the bright and/or hard large scale jet X-ray emission associated with powerful quasars has now been ruled out for six sources on the basis of over-predicting the observed gamma-ray flux. For each source presented in this paper, we found upper limits to the gamma-ray flux well below the levels predicted by the IC/CMB model using observations from the *Fermi*/LAT. For the sources not presented in this paper, 3C 273 and PKS 0637–752, previous *Fermi*/LAT observations showed similar IC/CMB-violating upper limits (Meyer & Georganopoulos 2014; Meyer et al. 2015, 2017). However, over-predicting the observed gamma-ray flux is not the only line of evidence against the IC/CMB model for these sources.

4.2. UV Upturns

In the case of PKS 1136–135, a high degree of UV polarization with fractional polarization measures in excess of 30% for several knots was detected in the rising second component of the jet SEDs (Cara et al. 2013). This implies a synchrotron origin for the second spectral component of these knots (see Atoyan & Dermer 2004; Harris et al. 2004; Kataoka & Stawarz 2005; Hardcastle 2006; Jester et al. 2006; Uchiyama et al. 2006), as the IC/CMB emission is expected to have very low polarization (see Uchiyama 2008; McNamara et al. 2009) while synchrotron radiation can be highly polarized. These UV-upturns in the knot SEDs are clearly seen in the case of knots A–C for PKS 2209+080 (shown in Figure 10) and knots α and A for PKS 1136–135 (shown in Figure 4). The optical spectrum for these knots is consistently harder than can be fit with a single power law from radio to optical, because the exponential cutoff occurs well before the optical. In these cases, fitting the UV-component of the SED with an IC/CMB model would predict much higher X-ray flux densities than are observed. Furthermore, knots α and A in PKS 1136–135 have a UV spectrum that is much harder than an IC/CMB model fit. These inconsistencies are additional lines of evidence against the IC/CMB model and imply another electron distribution
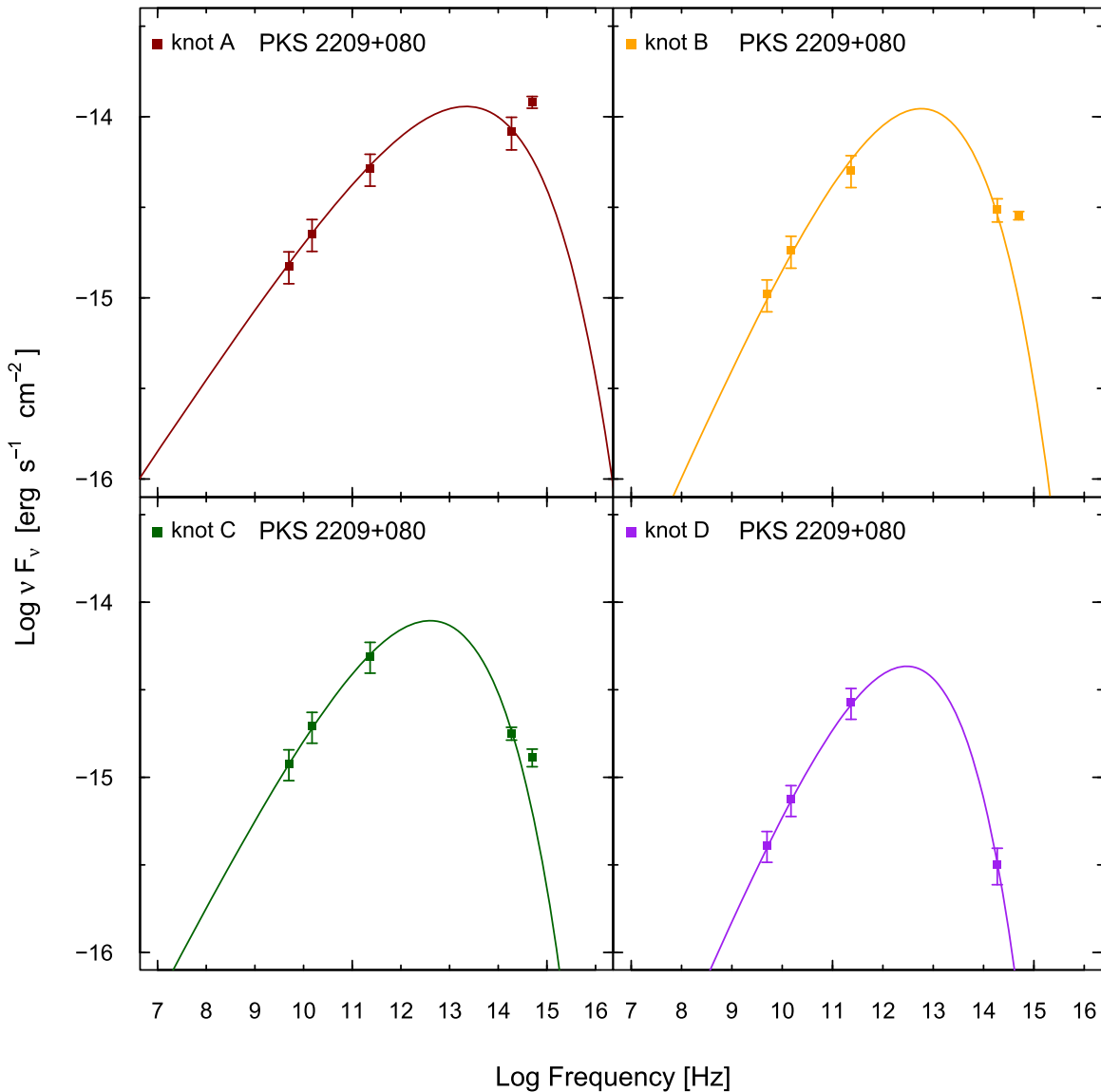
Figure 10. SEDs of knots A through D for PKS 2209+080. Single power-law fits with scaled exponential cutoffs are used to fit the radio data and first optical data point for each knot.

higher in energy to produce the UV-upturns and the X-ray emission.

4.3. Misalignment of the Non-IC/CMB Sources

The apparent misalignment of the sources is also in tension with the IC/CMB model. The IC/CMB model is able to reproduce the observed bright X-ray flux densities by requiring very small jet angles to the line of sight so the X-ray emission is highly relativistically beamed (Tavecchio et al. 2000; Celotti et al. 2001). It has been previously shown by Meyer et al. (2011) that blazars have a higher radio core dominance, R_{CE}, and lower crossing frequency, ν_{cross}, than radio galaxies. Figure 11, adapted from Meyer et al. (2011), shows the locations of all six sources in the R_{CE}–ν_{cross} plane in addition to other previously classified blazars and radio galaxies. As can be seen in Figure 11, our sources do not have the low crossing frequencies and high radio core dominances expected for highly aligned blazars. Additionally, PKS 1136–135 and PKS 2209+080 are well within the radio galaxy category,

suggesting they are fairly misaligned. It is also apparent from the total SEDs shown in Figure 2 that none of these sources have a Compton dominance greater than 1, which would be expected for highly aligned jets (see Figure 3 from Meyer et al. 2012).

4.4. X-Ray versus Radio Beaming Patterns

One property of the IC/CMB model is that it predicts a different relativistic beaming pattern than synchrotron emission. The expected beaming pattern for IC/CMB radiation is $L = L'\delta^{p+1+2\alpha_r}$, with $p = 2$ for a continuous flow and $p = 3$ for discrete moving blobs (Dermer 1995; Georganopoulos et al. 2001). Here, L is the luminosity in the galaxy frame assuming isotropy, L' is the solid-angle integrated luminosity in the jet frame, α_r is the radio spectral index, and δ is the Doppler factor. In the case of synchrotron emission, the expected beaming pattern is given by $L = L'\delta^{p+\alpha_r}$ (Dermer 1995).

Because larger angles of the jet to the line of sight decrease the value of δ, the observed IC/CMB flux should fall off faster
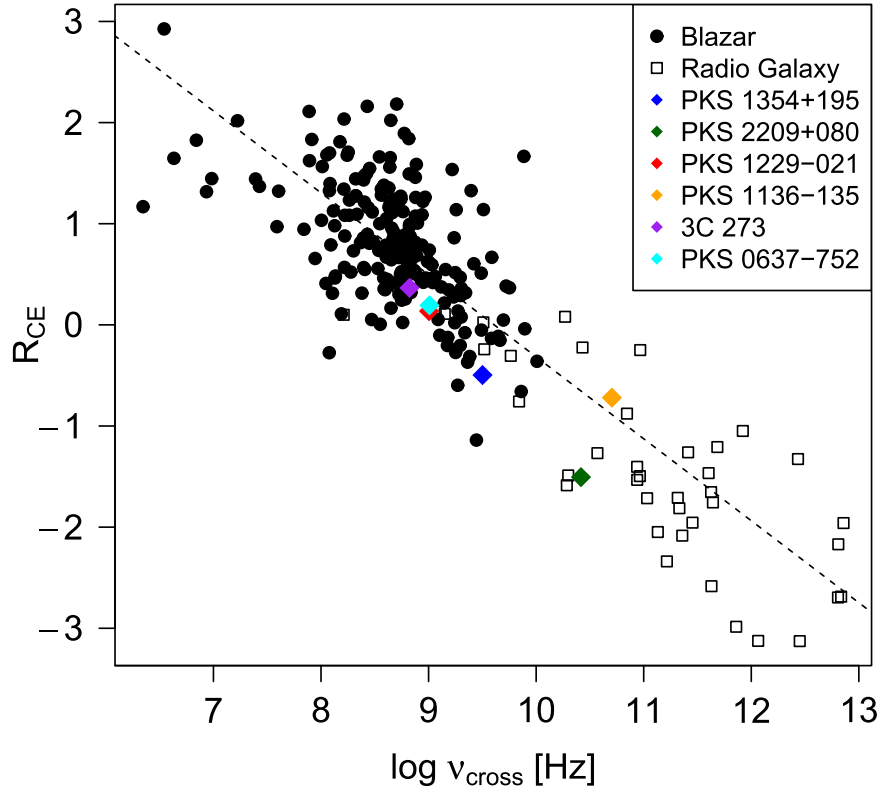
Figure 11. Plot adapted from Meyer et al. (2011). The radio core dominance, R_{CE}, plotted against ν_{cross}, the frequency at which the jet becomes dominant. Radio galaxies are shown as empty squares and blazars as filled circles. The broken line shown is the linear correlation between the plotted variables ($r = 0.87$). The six sources where we have now ruled out the IC/CMB model are plotted as diamonds.
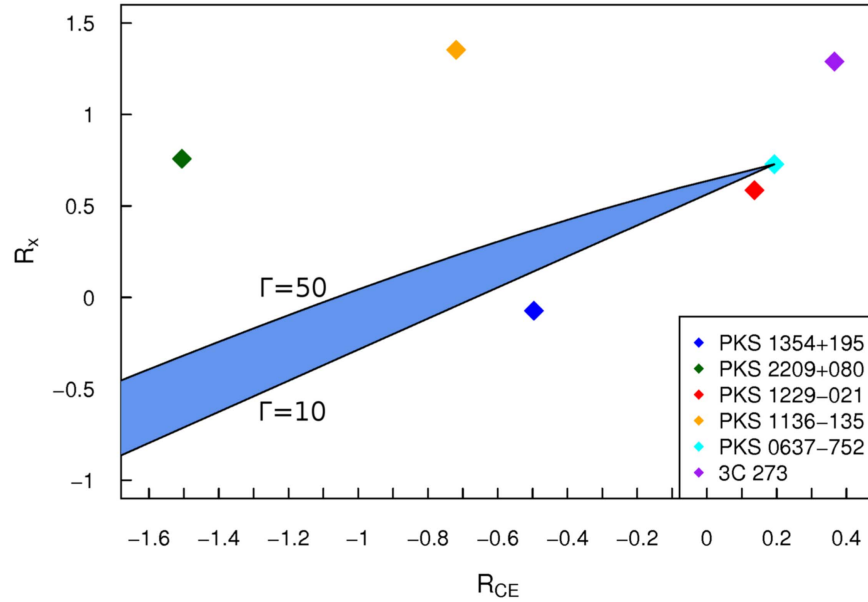

Figure 12. The X-ray dominance, R_x, plotted against the core dominance, R_{CE}, for the six sources where the IC/CMB model has now been ruled out shown as diamonds. Error bars are not shown, as they are on the order of the size of the data points. We plot R_x for the brightest X-ray knot in each source. Smaller values of R_{CE} correspond to more misaligned sources. The black lines show the expected result of misaligning the jet of PKS 0637–752, assuming an initial value of $\delta = 10$ for the knot with an initial misalignment of $5°73$. The upper and lower black lines show the cases where the Lorentz factor of the core is 50 and 10 respectively, with the blue shaded region showing the possible range between those values.

than the synchrotron flux as source misalignment increases due to the stronger dependence on δ of IC/CMB emission. We define a quantity we refer to as the X-ray dominance, R_x, as the logarithmic ratio of the 1 keV X-ray flux density to the 8.6 GHz radio flux density (in νF_ν). In Figure 12, we show the X-ray

dominance plotted against the core dominance for the X-ray brightest knots of the six sources in which IC/CMB is now ruled out as the X-ray emission mechanism, where the core dominance is a measure of the relative misalignment of the jet angle to the line of sight, as can be seen in Figure 11. Using the

above relativistic beaming equations for IC/CMB and synchrotron emission, it can be shown that $R_x \propto \delta_{\mathrm{knot}}^{1+\alpha_{\mathrm{knot}}}$ and $R_{\mathrm{CE}} \propto \delta_{\mathrm{core}}^{p+\alpha_{\mathrm{core}}}$. Using these equations, we plot the projected misalignment of PKS 0637–752 in Figure 12 as solid black curves, assuming $\alpha_{\mathrm{core}} = 0$, $\alpha_{\mathrm{knot}} = 0.7$, and $p = 2$ for the core, which reflects the most likely case in which the core is a standing shock and not a discrete moving feature. The misalignment curves are plotted for a core Γ of 10 and 50, with the shaded blue region representing the range of misalignment curves for a core Γ between 10 and 50. As can be seen in Figure 12, the other five sources do not fall within this misalignment zone of PKS 0637–752, as would be expected for the stronger beaming of the IC/CMB emission —albeit with a small sample of sources. The lack of correlation between R_x and R_{CE} suggests the radio-optical synchrotron emission and X-ray emission for these knots have the same relativistic beaming profile, not a different one as would be expected if the X-rays were produced by the IC/CMB mechanism. However, the large range in X-ray dominance also suggests that there is some intrinsic variability of the X-ray component within the sample. A larger sample should allow a more careful examination of the expected correlation, which we leave to future work.

4.5. Morphology and Host Properties of the Non-IC/CMB Sources

All of these sources show what we term a cannonball jet knot structure in the radio with quasi-periodic knot spacing. It has been suggested that this quasi-periodic spacing of the jet knots may be due to re-confinement shocks of the external medium, accretion disk instabilities, or a binary supermassive black hole (Godfrey et al. 2012). Other interesting characteristics of the radio morphology include the bright elongated structure at the end of the jet and lack of extended lobe emission for the sources 3C 273 (Bahcall et al. 1995) and PKS 1136–135 (though there is clearly lobe emission connected to the counter jet in PKS 1136–135), which may be identifiable with the "nose cone" jet structure seen in magnetohydrodynamics simulations. These nose cone structures are thought to occur when the jets are magnetically confined. Rather than the plasma deflecting back from the interface between the jet and intergalactic medium to form the lobes, it is collected in the end of the jet between the Mach disk and leading bow shock, forming the "nose cone." One observational signature associated with the nose cone jets is enhanced radio emission in the nose cone due to an enhanced magnetic field strength and thus synchrotron emissivity, but a decrease in the flux from higher energies due to a lack of particle acceleration in this region from shocks (see Clarke et al. 1986 for a discussion of nose cone jets). This observational characteristic appears to be true in the two cases of 3C 273 and PKS 1136–135, in which we can identify a possible nose cone structure.

The host galaxy of PKS 2209+080, which is visible in our *HST* observations, shows a clear tidal tail structure that is suggestive of the galaxy having undergone a recent merger. The disturbed elliptical host galaxy of 3C 273 has also shown some evidence of being in a recent merger (Martel et al. 2003). These findings are consistent with the work by Chiaberge et al. (2015), suggesting that all radio-loud AGN have undergone major recent mergers.

4.6. Alternatives to IC/CMB

One emission mechanism that has not been ruled out for the X-rays in MSC jets is synchrotron radiation from a second higher-energy population of electrons. If these X-ray knots are due to a second electron energy distribution, this means that these jets can exhibit highly efficient in situ particle acceleration very far from the central engine (on the order of kpcs). These electrons would need to be highly energetic (at a few to hundreds of TeV energies), and in cases where the IR/optical flux is totally consistent with a single spectrum from radio to optical, have a lower energy cutoff such that they do not overproduce the observed IR/optical emission. One consequence of these multi-TeV energy electrons is that they should IC scatter the CMB to TeV gamma-rays, which may be detectable with the upcoming CTA for low-redshift sources (Georganopoulos et al. 2006; Meyer et al. 2015).

Alternatively, it is possible these X-rays are due to hadronic emission processes whereby the X-rays are produced by direct proton synchrotron radiation or from the synchrotron radiation produced by secondary electrons resulting from photo-hadronic interactions like the Bethe–Heitler process or photopion production (see Bhattacharyya & Gupta 2016; Kusunose & Takahara 2017; Petropoulou et al. 2017). Like synchrotron models, and unlike IC/CMB, hadronic models are highly tunable and can be made to reproduce most observed SEDs because there are a large number of parameters to adjust. However, one distinguishing characteristic of hadronic models would be the expected neutrino emission from charged pion or neutron decay resulting from interactions between high-energy protons and photons (Mannheim & Biermann 1989). It has been claimed that the bright gamma-ray flare observed in the blazar PKS B1424-418 is hadronic in nature, due to the detection of a PeV-energy neutrino with a high degree of positional and temporal coincidence (Kadler et al. 2016) by the IceCube neutrino detector. However, the detection rate of IceCube high-energy neutrinos is so low that this is not expected to be a very robust means of distinguishing between hadronic and leptonic models for blazars. Additionally, in the case of PKS 0637–752, hadronic emission models require highly super-Eddington jet powers (Kusunose & Takahara 2017).

These models for the X-ray emission do not have many of the problematic features of the IC/CMB model. They do not require these jets to remain highly relativistic on large scales or be highly aligned. The observed "knottiness" of these X-ray jets is well-explained by the much stronger radiative losses for these emission mechanisms. Finally, the second synchrotron model naturally explains the high degrees of polarization measured in the UV-upturns for PKS 1136–135 (Cara et al. 2013) and 3C 273 (Jester et al. 2007).

5. Summary and Conclusions

In this paper, we have shown that the IC/CMB model cannot explain the X-ray emission for the large-scale MSC jets of the powerful quasars PKS 1136–135, PKS 1229–021, PKS 1354 +195, and PKS 2209+080 at the 14.3σ, 6.1σ, 4.7σ, and $>15.2\sigma$ levels, respectively. The IC/CMB model was ruled out due to IC/CMB violating gamma-ray upper limits with the *Fermi*/LAT, where the predicted IC gamma-ray flux is fixed by the requirement of fitting the observed X-ray flux density with the IC/CMB model. In the case of PKS 1136–135, knots α and A also show a steeply rising optical spectrum, which would

predict much higher X-ray flux densities than observed if fit with an IC/CMB model. These sources now represent an addition of three to the list of MSC jets where the IC/CMB model has already been conclusively ruled out: PKS 0637–752, 3C 273, and PKS 1136–135 (PKS 1136–135 has already been ruled out on the basis of UV polarization). Furthermore, our *HST* observations for PKS 2209+080 show a newly detected optical jet with possible tidal tails in the host galaxy. Based on the radio core dominance and crossing frequencies of PKS 1136–135 and PKS 2209+080, we have shown that these jets must be fairly misaligned—not extremely well-aligned blazars, as would be required under the IC/CMB model. Because these results lead us to reject the IC/CMB model as the emission mechanism for these MSC jets, we must consider alternative emission mechanisms, such as a second population of electrons producing a second synchrotron component or hadronic emission models. In the case of the second synchrotron model, it would be important to understand how the high-energy electron distribution is created and what mechanisms might give rise to such highly efficient particle acceleration in situ kpcs from the central engine.

Appendix

A.1. Synchrotron Fits

The empirical fits to the observed synchrotron SEDs are simple power laws with scaled exponential cutoffs, corresponding to a simple power-law electron energy distribution with maximum Lorentz factor. They have the following form:

$$\nu f_\nu = N \left(\frac{\nu}{10^{10}\,\mathrm{Hz}} \right)^\gamma \exp\left(-\left(\frac{\nu}{\nu_1} \right)^\beta \right). \quad (1)$$

In this equation, ν is the observed frequency of the radiation, γ the power-law index, ν_1 the frequency at which the exponential turnover begins, β the steepness of the cutoff, and N is the normalization of the spectrum, which has the units $\mathrm{erg\,cm^{-2}\,s^{-1}}$.

A.2. IC/CMB Shifting Equations

The IC/CMB model has the following form for the shifting in luminosity and frequency of the lower-energy synchrotron spectrum, first derived in Georganopoulos et al. (2006):

$$\frac{\nu_c}{\nu_s} = \frac{\nu_{\mathrm{CMB}}}{e(B/\delta)/[2\pi m_e c(1+z)]} \quad (2)$$

$$\frac{L_c}{L_s} = \frac{32 U_{\mathrm{CMB}}(1+z)^4}{3(B/\delta)^2}, \quad (3)$$

where B is the magnetic field strength, e is the elementary charge, U_{CMB} is the CMB energy density at the current epoch, ν_{CMB} the CMB peak frequency at the current epoch, z is the redshift, m_e is the electron mass, c is the speed of light, and δ is the Doppler factor. Note that the only free parameter in this shift is B/δ which becomes fixed upon fitting the X-ray component of the SED. If one assumes an equipartition magnetic field, this shift is only parametrized by δ. Also note that these shifts should preserve the same spectral index for both the synchrotron and inverse-Compton components, although this is not always seen for these MSC jets.

ORCID iDs

Eileen T. Meyer ⓘ https://orcid.org/0000-0002-7676-9962
Markos Georganopoulos ⓘ https://orcid.org/0000-0002-2040-8666

References

Aharonian, F. A. 2002, MNRAS, 332, 215
Arshakian, T. G., & Longair, M. S. 2004, MNRAS, 351, 727
Atoyan, A., & Dermer, C. D. 2004, ApJ, 613, 151
Bahcall, J. N., Kirhakos, S., Schneider, D. P., et al. 1995, ApJL, 452, L91
Bhattacharyya, W., & Gupta, N. 2016, ApJ, 817, 121
Cara, M., Perlman, E. S., Uchiyama, Y., et al. 2013, ApJ, 773, 186
Cavagnolo, K. W., McNamara, B. R., Nulsen, P. E. J., et al. 2010, ApJ, 720, 1066
Celotti, A., Ghisellini, G., & Chiaberge, M. 2001, MNRAS, 321, L1
Chartas, G., Worrall, D. M., Birkinshaw, M., et al. 2000, ApJ, 542, 655
Chen, Y. Y., Zhang, X., Zhang, H. J., & Yu, X. L. 2015, MNRAS, 451, 4193
Chiaberge, M., Gilli, R., Lotz, J. M., & Norman, C. 2015, ApJ, 806, 147
Chiaberge, M., & Marconi, A. 2011, MNRAS, 416, 917
Clarke, D. A., Norman, M. L., & Burns, J. O. 1986, ApJL, 311, L63
Clautice, D., Perlman, E. S., Georganopoulos, M., et al. 2016, ApJ, 826, 109
Dermer, C. D. 1995, ApJL, 446, L63
Dermer, C. D., & Atoyan, A. 2004, ApJL, 611, L9
Fanaroff, B. L., & Riley, J. M. 1974, MNRAS, 167, 31P
Georganopoulos, M., Kirk, J. G., & Mastichiadis, A. 2001, ApJ, 561, 111
Georganopoulos, M., Perlman, E. S., Kazanas, D., & McEnery, J. 2006, ApJL, 653, L5
Godfrey, L. E. H., Lovell, J. E. J., Burke-Spolaor, S., et al. 2012, ApJL, 758, L27
Hardcastle, M. J. 2006, MNRAS, 366, 1465
Hardcastle, M. J., Lenc, E., Birkinshaw, M., et al. 2016, MNRAS, 455, 3526
Harris, D. E., Lee, N. P., Schwartz, D. A., et al. 2017, ApJ, 846, 119
Harris, D. E., & Krawczynski, H. 2006, ARA&A, 44, 463
Harris, D. E., Mossman, A. E., & Walker, R. C. 2004, ApJ, 615, 161
Jester, S., Harris, D. E., Marshall, H. L., & Meisenheimer, K. 2006, ApJ, 648, 900
Jester, S., Meisenheimer, K., Martel, A. R., Perlman, E. S., & Sparks, W. B. 2007, MNRAS, 380, 828
Jorstad, S. G., & Marscher, A. P. 2006, AN, 327, 227
Jorstad, S. G., Marscher, A. P., Lister, M. L., et al. 2005, AJ, 130, 1418
Kadler, M., Krauß, F., Mannheim, K., et al. 2016, NatPh, 12, 807
Kataoka, J., & Stawarz, Ł. 2005, ApJ, 622, 797
Kharb, P., Lister, M. L., Marshall, H. L., & Hogan, B. S. 2012, ApJ, 748, 81
Kim, D., Im, M., Kim, J. H., et al. 2015, ApJS, 216, 17
Kusunose, M., & Takahara, F. 2017, ApJ, 835, 20
Lister, M. L., Aller, M. F., Aller, H. D., et al. 2016, AJ, 152, 12
Lister, M. L., Cohen, M. H., Homan, D. C., et al. 2009, AJ, 138, 1874
Liu, Y., Jiang, D. R., & Gu, M. F. 2006, ApJ, 637, 669

Lovell, J. E. J., Tingay, S. J., Piner, B. G., et al. 2000, in Astrophysical Phenomena Revealed by Space VLBI, ed. H. Hirabayashi, P. G. Edwards, & D. W. Murphy (Sagamihara City: ISAS), 215

Mannheim, K., & Biermann, P. L. 1989, A&A, 221, 211

Marshall, H. L., Gelbord, J. M., Schwartz, D. A., et al. 2011, ApJS, 193, 15

Martel, A. R., Ford, H. C., Tran, H. D., et al. 2003, AJ, 125, 2964

McNamara, A. L., Kuncic, Z., & Wu, K. 2009, MNRAS, 395, 1507

Mertens, F., & Lobanov, A. 2015, A&A, 574, A67

Mertens, F., & Lobanov, A. P. 2016, A&A, 587, A52

Meyer, E. T., Breiding, P., Georganopoulos, M., et al. 2017, ApJL, 835, L35

Meyer, E. T., Fossati, G., Georganopoulos, M., & Lister, M. L. 2011, ApJ, 740, 98

Meyer, E. T., Fossati, G., Georganopoulos, M., & Lister, M. L. 2012, ApJL, 752, L4

Meyer, E. T., & Georganopoulos, M. 2014, ApJL, 780, L27

Meyer, E. T., Georganopoulos, M., Sparks, W. B., et al. 2015, ApJ, 805, 154

Meyer, E. T., Sparks, W. B., Georganopoulos, M., et al. 2016, ApJ, 818, 195

Miller, B. P., Brandt, W. N., Gallagher, S. C., et al. 2006, ApJ, 652, 163

Mullin, L. M., & Hardcastle, M. J. 2009, MNRAS, 398, 1989

Perlman, E. S., Georganopoulos, M., Marshall, H. L., et al. 2011, ApJ, 739, 65

Petropoulou, M., Vasilopoulos, G., & Giannios, D. 2017, MNRAS, 464, 2213

Sambruna, R. M., Gambill, J. K., Maraschi, L., et al. 2004, ApJ, 608, 698

Sambruna, R. M., Gliozzi, M., Donato, D., et al. 2006, ApJ, 641, 717

Sambruna, R. M., Maraschi, L., Tavecchio, F., et al. 2002, ApJ, 571, 206

Schwartz, D. A., Marshall, H. L., Lovell, J. E. J., et al. 2000, ApJL, 540, 69

Stanley, E. C., Kharb, P., Lister, M. L., et al. 2015, ApJ, 807, 48

Stawarz, Ł., Sikora, M., Ostrowski, M., & Begelman, M. C. 2004, ApJ, 608, 95

Tavecchio, F., Ghisellini, G., & Celotti, A. 2003, A&A, 403, 83

Tavecchio, F., Maraschi, L., Sambruna, R. M., & Urry, C. M. 2000, ApJL, 544, L23

Tavecchio, F., Maraschi, L., Wolter, A., et al. 2007, ApJ, 662, 900

Uchiyama, Y. 2008, IJMPD, 17, 1475

Uchiyama, Y., Urry, C. M., Cheung, C. C., et al. 2006, ApJ, 648, 910

Wilson, A. S., & Yang, Y. 2002, ApJ, 568, 133